RSC Advances

PAPER

View Article Online
View Journal | View Issue

Cite this: *RSC Adv.*, 2015, **5**, 83408

Carbon@$NiCo_2S_4$ nanorods: an excellent electrode material for supercapacitors†

Laiquan Li, Ziyang Dai, Yufei Zhang, Jun Yang, Wei Huang* and Xiaochen Dong*

Received 29th July 2015
Accepted 17th September 2015

DOI: 10.1039/c5ra15022a

www.rsc.org/advances

Carbon@$NiCo_2S_4$ nanorods were synthesized through a facile *in situ* hydrothermal approach using carbon supported nickel (Ni/C) nanorods as both the template and nickel source. The morphology and electrochemical properties of $NiCo_2S_4$ can be effectively tuned with carbon nanorods as well as the addition of hydrogen peroxide (H_2O_2) during the hydrothermal process. The carbon nanorod endows $NiCo_2S_4$ with rod-like morphology and good electrochemical stability during active reversible redox reactions. Moreover, the addition of H_2O_2 creates the porous structure of $NiCo_2S_4$, improving its electrochemically active surface area greatly, which is beneficial for efficient charge and ion transport in electrodes. Electrochemical measurements indicate that the H_2O_2 treated carbon@$NiCo_2S_4$ (labeled as C@$NiCo_2S_4$–H) nanorods present high specific capacitance (1455 F g^{-1} at the current density of 1 A g^{-1}) and excellent cycling stability (83% retention after 2000 cycles). It is believed that other carbon-based composites with superior electrochemical behavior for supercapacitor applications can also be synthesized using the proposed method in this study.

Introduction

Fossil fuels (coal, oil and gas) are rapidly being depleted and energy crisis is becoming a serious issue faced by the entire humanity today. With the exploration and implementation of renewable resources booming across the world, the accompanying development of energy storage technologies is receiving unprecedented challenges. Supercapacitors, which emerged as a new generation of energy storage and conversion devices, show promising application potential attributed to their high energy density, fast recharging capabilities and stable cyclability.[1–4] In general, supercapacitors can be classified into electric double layer supercapacitors (EDLCs) and pseudocapacitors based on different charge storage mechanisms.[5,6] The electric double layer supercapacitors usually consist of carbon materials, which have large specific surface area, super conductivity and long cycling lifetimes.[7] Moreover, pseudocapacitors exhibit much higher specific capacitance due to the reversible faradaic redox reactions. Transition metal oxides combining the virtues of two different metals are generally used as electrode materials for high-performance pseudocapacitors.[8] Compared with carbon materials, transition metal oxides, such as $NiCo_2O_4$,[9,10] $MnCo_2O_4$,[11,12] $NiMoO_4$,[13,14] usually possess higher specific capacitance but poorer rate performance and inferior cycling stability. The combination of pseudocapacitive materials with carbon materials (such as graphene,[15] carbon nanotubes,[16] and porous carbon materials[17,18]) is a promising strategy to address this issue.

More recently, illuminated by the excellent electrochemical performance of metal oxides, transition metal sulfides have been excavated as a new class of pseudocapacitive materials due to their higher power density, compared to that of metal oxides.[19] For example, it has been reported that $NiCo_2S_4$ possesses better conductivity than $NiCo_2O_4$.[20] However, $NiCo_2S_4$ is still subjected to relatively poor electrochemical performance due to its intrinsically low surface area and non-porosity.[15] To overcome this problem, various efforts have been made to synthesize metal sulfides with large surface areas such as nanosheets,[21] nanowires,[22,23] and nanotubes.[24] Recently, it was reported that Ni/C nanorods can serve as a template for the synthesis of a $NiCo_2O_4$/carbon nanorod composite.[25] However, it is still a great challenge to obtain carbon@$NiCo_2S_4$ composites with better conductivity and higher porosity.

Herein, we proposed a facile hydrothermal approach for the synthesis of C@$NiCo_2S_4$ nanorods using Ni/C nanorods simultaneously as the structural support and nickel source. The electron microscopy (SEM, TEM) measurements suggest that the composite has a rod-like morphology similar to that of the Ni/C nanorod. More importantly, the addition of H_2O_2 can significantly improve the porosity of $NiCo_2S_4$, hence greatly increasing its electrochemically active surface area. Owing to the significantly improved electrochemical properties, the as-prepared composite electrode not only demonstrated a high specific capacitance (1455 F g^{-1}) at the current density of 1.0 A g^{-1}, but also showed excellent cycling stability.

Key Laboratory of Flexible Electronics (KLOFE) & Institute of Advanced Materials (IAM), Jiangsu National Synergistic Innovation Center for Advanced Materials (SICAM), Nanjing Tech University (Nanjing Tech), 30 South Puzhu Road, Nanjing 211816, China. E-mail: iamxcdong@njtech.edu.cn; iamwhuang@njtech.edu.cn

† Electronic supplementary information (ESI) available. See DOI: 10.1039/c5ra15022a

Experiment section

Preparation of Ni/C nanorod

All chemicals are of analytical grade and used without any further treatment. The Ni/C nanorod was synthesized according to the method reported in a previous study in the literature.[26] In a typical experiment, 0.28 g of dimethylglyoxime was dissolved in 24 ml of ethanol. The pH value of the resulting solution was adjusted to 13 with 0.5 M NaOH. The mixture was then dropped into 800 ml of deionized water containing 0.52 g of $NiCl_2 \cdot 6H_2O$ under vigorous stirring. The red floccule formed during the reaction was then collected and thoroughly washed with deionized water and absolute alcohol several times, followed by vacuum-drying at 80 °C for 6 h. Finally, the collected red floccule was calcined at 350 °C for 0.5 h in an argon atmosphere with a heating rate of 1 °C min^{-1} to obtain the rod-like Ni/C composite. The weight percentage of Ni in the Ni/C nanorod was calculated to be around 53% according to the molecular weight of C in dimethylglyoxime and Ni in $NiCl_2 \cdot 6H_2O$.

Synthesis of C@$NiCo_2S_4$–H nanorod

The C@$NiCo_2S_4$–H nanorod was synthesized by an *in situ* hydrothermal method. Briefly, 40 mg of Ni/C nanorods, 0.4 g of urea and 170 mg of $CoCl_2 \cdot 6H_2O$ were dissolved into 33 ml of DI water with continuous stirring for 30 min, followed by the addition of 2 ml of 30 wt% H_2O_2. Then, the mixture was transferred to a 50 ml Teflon-lined steel autoclave and kept at 180 °C for 12 h. Furthermore, the dark pink precursor was obtained by filtration and dried at 80 °C overnight. Then, 21 mg of the collected precursor and 120 mg of Na_2S were dispersed in 30 ml of DI water under magnetic stirring. The mixture was further transferred to a 50 ml Teflon-lined steel autoclave and maintained at 180 °C for 6 h. The black precipitates were collected and washed with deionized water and absolute alcohol, and they were dried at 80 °C for 12 h to obtain the C@$NiCo_2S_4$–H nanorods. The C@$NiCo_2S_4$ nanorod without H_2O_2 was synthesized with the same process except for the addition of H_2O_2. For comparison, the $NiCo_2S_4$ nanorod was synthesized according to the literature.[27]

Characterization

The crystal structures of the samples were examined by X-ray diffraction (XRD, Bruker D8 Advance) with Cu-Kα radiation (1.5418 Å) operating at 40 kV and 100 mA. The morphologies of the samples were studied using field-emission scanning electron microscopy (FESEM; Hitachi, S-4800, Japan) and transmission electron microscopy (TEM, JEOL JEM-2010). The Brunauer–Emmett–Teller (BET) method was used to calculate the specific surface area of the samples by nitrogen adsorption–desorption measurement on an ASAP 2460 (Micromeritics, USA).

Electrochemical measurements

Electrochemical measurements were carried out with a CHI 760D electrochemical workstation (CH Instruments) with a saturated Ag/AgCl as reference electrode, a Pt plate as counter electrode and C@$NiCo_2S_4$ nanorod samples as working electrode. A 6.0 M KOH aqueous solution was used as the electrolyte. To prepare the working electrodes, the C@$NiCo_2S_4$ nanorod sample, acetylene black and PVDF were used as the active material, conductive agent and binder with a weight ratio of 8 : 1 : 1, respectively. The electrode paste was coated onto nickel foam with a calculated mass loading of about 1.0 mg. The performance of the supercapacitor was evaluated by cyclic voltammetry (CV), galvanostatic charge–discharge tests, and electrochemical impedance spectroscopy (EIS) measurements (1–100 000 Hz).

Results and discussion

Fig. 1 shows the XRD patterns of Ni/C, C@$NiCo_2S_4$ and C@$NiCo_2S_4$–H nanorod samples. For the Ni/C nanorod, there are two distinct diffraction peaks at 44.4° and 51.8°, which can be attributed to (111) and (200) diffraction planes of nickel, respectively. The broad peak at 26° corresponds to the amorphous carbon, indicating the formation of the Ni/C composite. For the C@$NiCo_2S_4$ and C@$NiCo_2S_4$–H nanorod samples, the diffraction peaks at 26.8°, 31.6°, 38.3°, 50.5°, and 55.3° can be indexed to the (220), (311), (400), (511), and (440) facets of the $NiCo_2S_4$ phase (JCPDS 20-0782), respectively. Furthermore, the energy dispersive X-ray spectrometry (EDS) results confirmed that the atomic ratio of Ni : Co is around 1 : 2 (Fig. S1†). It is noteworthy to mention that there are no significant differences between the two XRD patterns, suggesting that the addition of H_2O_2 has no obvious effect on the crystal phase of the as-fabricated composites.

The morphologies of the Ni/C and C@$NiCo_2S_4$ nanorod samples were characterized by field-emission scanning electron microscopy (FESEM), as shown in Fig. 2a–d. Fig. 2a shows that Ni/C presents nanorod structures with smooth surfaces and diameters around 100–200 nm. Compared with a Ni/C nanorod, a C@$NiCo_2S_4$ nanorod exhibits a rough surface and nanoparticles can be clearly seen on its surface, as shown in Fig. 2b.

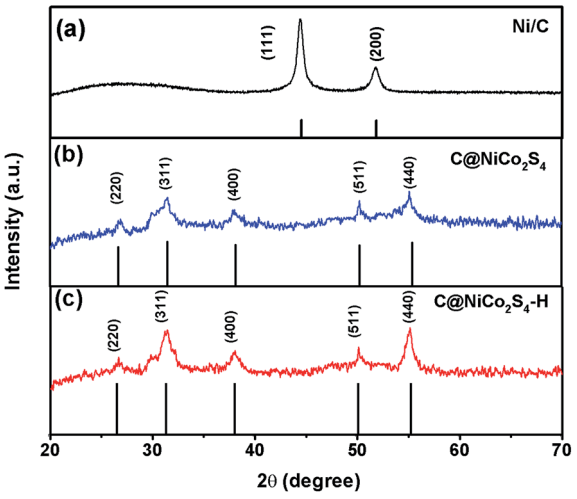

Fig. 1 XRD patterns of (a) Ni/C, (b) C@$NiCo_2S_4$, and (c) C@$NiCo_2S_4$–H nanorods.

This observation indicates that Ni in the Ni/C nanorod can directly react with the Co^{2+} adsorbed on the surface of the Ni/C nanorod and form a carbon nanorod supported Ni–Co precursor. In this case, the fixed nickel sites can not only enhance the dispersion of the active material, but also allow full utilization of nickel for the formation of $NiCo_2S_4$. At the same time, the conductivity of the composite can be significantly improved by the existing carbon network.[28]

With the addition of H_2O_2, the surface of the C@$NiCo_2S_4$–H nanorod becomes rougher compared with that of the C@$NiCo_2S_4$ nanorod, as depicted in Fig. 2c and d. This can be explained by the fact that the Ni nanoparticles on the surface of the Ni/C nanorod can be oxidized into Ni^{2+} by the strong oxidizer H_2O_2. Moreover, the continuous infiltration of H_2O_2 into the Ni/C nanorod can further corrode the deeper region of the structure, hence leading to the formation of a thinner Ni/C nanorod.[29] In addition, a large amount of oxygen could be generated by H_2O_2 with the increasing temperature, resulting in the porous structure of $NiCo_2S_4$. Fig. 2e–i shows the SEM and energy dispersive X-ray (EDX) elemental mapping images of C@$NiCo_2S_4$–H nanorods. It can be clearly seen that all the compositional elements, namely, C, Co, Ni and S, are uniformly distributed across the detected region, suggesting uniform C@$NiCo_2S_4$ nanorods were successfully synthesized.

TEM measurements provide further insight into the morphology and detailed crystal structure of the as-obtained C@$NiCo_2S_4$–H nanorod. As shown in Fig. 3a, the sample exhibits a nanorod structure with a rough surface, which is consistent with the previous SEM observation. It can be clearly seen that the carbon nanorod was uniformly wrapped in $NiCo_2S_4$ with thickness of about 20–40 nm. Fig. 3b shows the high-resolution TEM image of the sample. Different lattice fringes corresponding to different interplanar spacings can be clearly observed. The 0.54 nm, 0.28 nm and 0.23 nm interplanar spacings labeled in Fig. 3b can be accurately assigned to the (111), (311) and (400) planes of $NiCo_2S_4$.

Specific surface area is a key factor that influences electrolyte ion diffusion and electron transport, which are important in determining the electrochemical performance. Nitrogen adsorption–desorption isotherms of C@$NiCo_2S_4$ and C@$NiCo_2S_4$–H samples are shown in Fig. 4a and b, respectively. The obvious hysteresis loop indicates that both of the resultant

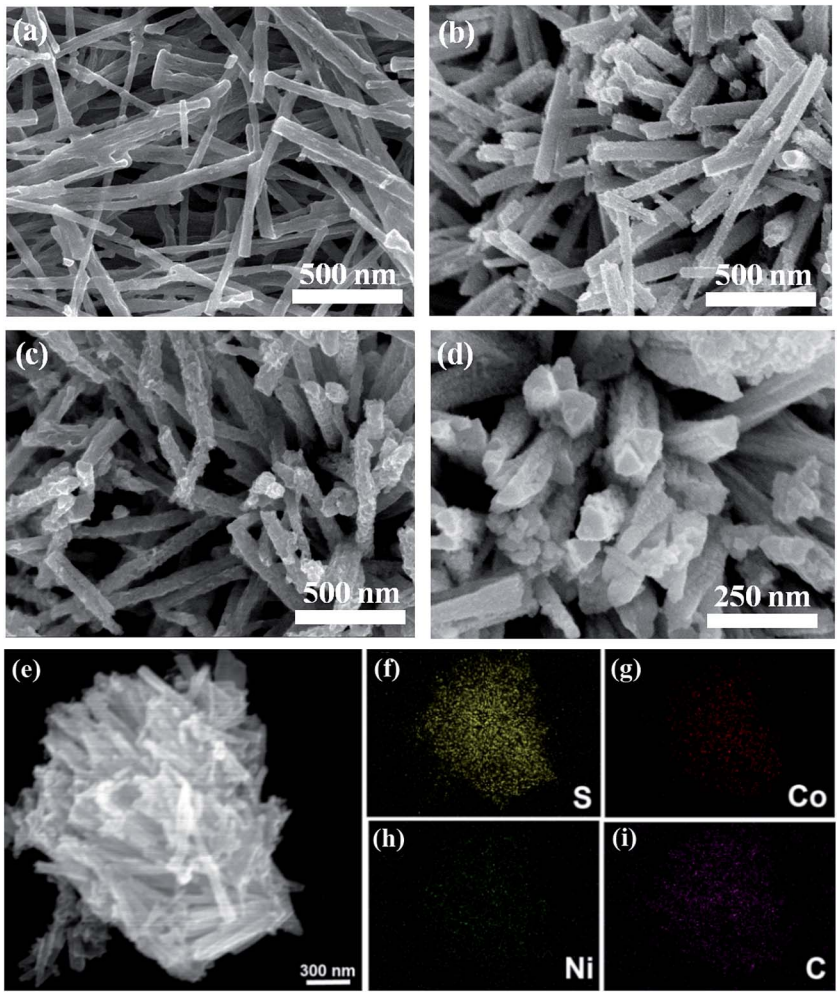

Fig. 2 SEM images of (a) Ni/C nanorods, (b) C@$NiCo_2S_4$ nanorods, and (c and d) C@$NiCo_2S_4$–H nanorods at different magnifications. (e) SEM image of C@$NiCo_2S_4$–H nanorods and their corresponding EDX elemental mappings: (f) S, (g) Co, (h) Ni, and (i) C elements.

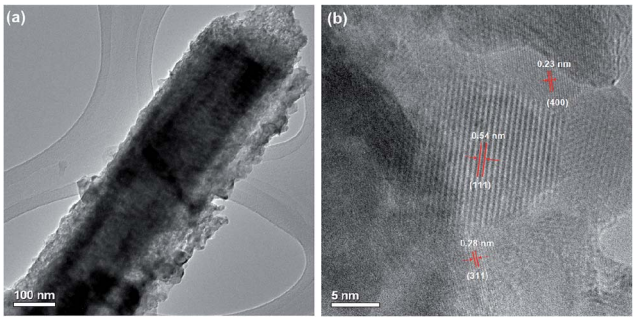

Fig. 3 TEM and HR-TEM images of C@$NiCo_2S_4$–H nanorod.

composites possess mesoporous characteristics. It can be noted that the addition of H_2O_2 can enhance the specific surface area of the C@$NiCo_2S_4$ nanorod from 20.6 to 39.2 $m^2\ g^{-1}$. The pore size distribution further indicates that the C@$NiCo_2S_4$–H nanorod possesses a large pore diameter (Fig. S2†). It can be concluded that H_2O_2 plays an important role in forming the mesoporous structures as well as enlarging specific surface area.

Electrochemical properties

To systematically investigate the electrochemical performance, cyclic voltammetry (CV) and galvanostatic charge–discharge measurements of the different samples were carried out using 6.0 M KOH solution as the electrolyte. Fig. 5a shows the *CV* curves of C@$NiCo_2S_4$ nanorod samples at a scan rate of 50 mV s^{-1}. A pair of redox peaks can be clearly observed during the anodic and cathodic sweeps, originating from faradaic reactions within the electrode that can be described by the following equations:[16,30,31]

$$NiCo_2S_4 + OH^- + H_2O \leftrightarrow NiSOH + 2CoSOH + 2e^- \quad (1)$$

$$CoSOH + OH^- \leftrightarrow CoSO + H_2O + e^- \quad (2)$$

As expected, the C@$NiCo_2S_4$–H nanorod presents a much larger enclosed area of the *CV* curve than that of the composite prepared without H_2O_2, indicating its higher capacitance. Fig. 5b shows the charge–discharge curves of the C@$NiCo_2S_4$ nanorod at a current density of 1.0 A g^{-1}. The discharge curves exhibit a typical pseudocapacitive feature, which is obviously different from the linear characteristics of electric double layer capacitors.[32] The specific capacitance can be calculated from the following equation:[33]

$$C_s = I\Delta t/m\Delta V$$

where I (A) is the discharge current, Δt (s) is the discharge time, m (g) is the mass of the active material and ΔV (V) is the voltage window for the charge–discharge process. Based on this equation, the specific capacitance of the C@$NiCo_2S_4$–H nanorod reaches 1455 F g^{-1}, whereas that of the C@$NiCo_2S_4$ nanorod is only 738.9 F g^{-1}. This may be attributed to the large specific surface area and porous structure of H_2O_2-treated $NiCo_2S_4$, which provides effective pathways for electrolyte ion diffusion and electron transport. Moreover, the carbon nanorod can greatly enhance the conductivity of the composite, thus leading to ultrafast faradaic reactions during the charge–discharge process.

Fig. 6a shows the *CV* curves of the C@$NiCo_2S_4$–H nanorod at the scan rates from 2 to 30 mV s^{-1}. A distinct pair of redox peaks can be clearly observed even at a scan rate as high as 30 mV s^{-1}, indicating a good pseudocapacitive nature for $NiCo_2S_4$. In addition, the peak current increases with the scan rate, demonstrating the small equivalent series resistance under a rapid charge–discharge process.[34] Fig. 6b presents the charge–discharge curves of the C@$NiCo_2S_4$–H nanorods, and the plateau regions in the discharge curves further demonstrate that the capacitive characteristics are mainly governed by faradaic redox reactions.[35] The specific capacitance values are 1455, 1353, 1326 and 1262 F g^{-1} at current densities of 1.0, 2.0, 4.0 and 10.0 A g^{-1}, respectively. Even at a current density of 20.0 A g^{-1}, the specific capacitance of the C@$NiCo_2S_4$–H nanorods can still reach an impressive value of 1182 F g^{-1}. Fig. 6c shows the specific capacitance values at different discharge current densities. It can be observed that the specific capacitance of the C@$NiCo_2S_4$–H nanorods is much higher than that of the C@$NiCo_2S_4$ nanorods at different current densities. Furthermore, $NiCo_2S_4$ nanorods were synthesized for comparison (Fig. S3†). The lower specific capacitance indicates that the addition of carbon materials can greatly enhance its electrochemical performance.

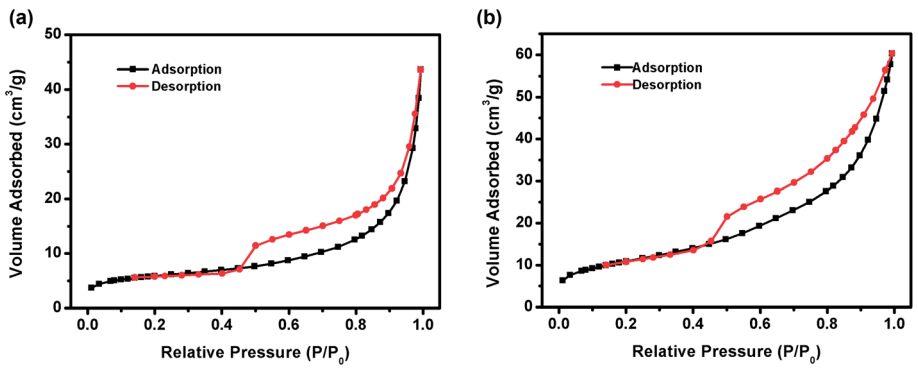

Fig. 4 Nitrogen adsorption–desorption isotherms of (a) C@$NiCo_2S_4$ and (b) C@$NiCo_2S_4$–H nanorods.

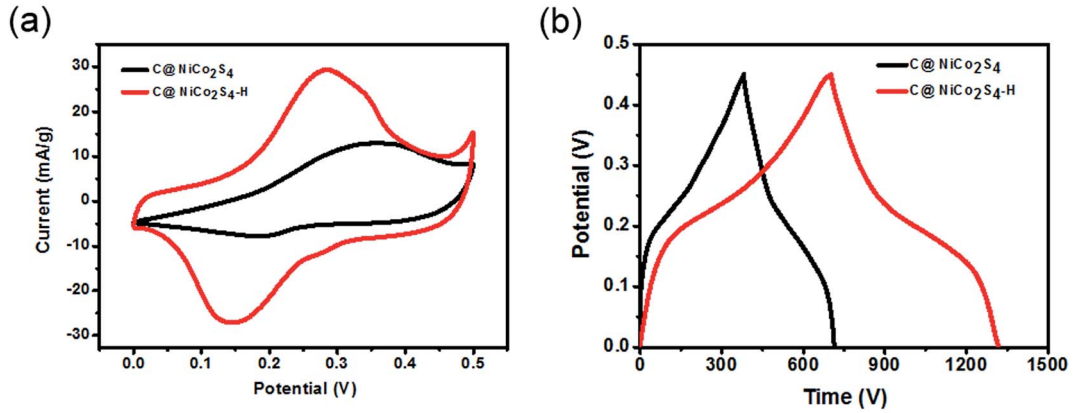

Fig. 5 (a) *CV* curves of C@$NiCo_2S_4$ and C@$NiCo_2S_4$–H nanorod samples at the scan rate of 50 mV s^{-1}. (b) Charge–discharge curves of C@$NiCo_2S_4$ and C@$NiCo_2S_4$–H nanorod samples at the current density of 1.0 A g^{-1}.

Fig. 6d presents the cycling performance of C@$NiCo_2S_4$–H nanorods at a current density of 20 A g^{-1}; it indicates that the electrode presents excellent cycling stability and retained ~83% of the initial capacitance even after 2000 cycles, which is better than many previously reported $NiCo_2S_4$ nanomaterials.[36,37] The excellent stability of the electrode may be attributed to the synergistic effect of the carbon nanorods and $NiCo_2S_4$. Moreover, the carbon nanorod can maintain the structure of $NiCo_2S_4$ stable during active reversible redox reactions. The inset of Fig. 6d shows the discharge–charge curves, indicating that the symmetrical discharge–charge curves remain even after 2000 cycles.

Fig. 7a shows the Nyquist plots of C@$NiCo_2S_4$ and C@$NiCo_2S_4$–H nanorod samples carried out at frequency range from 1 Hz to 10 kHz. As shown by the inset of Fig. 7a, EIS can be fitted by an equivalent circuit, which is composed of an internal resistance R_s, an interfacial charge transfer resistance R_{ct}, a Warburg resistance W, and a constant phase element for the double layer capacitance. The internal resistance (R_s) of the samples can be estimated from the intercept of the semicircle on the X-axis at a high frequency.[38] As illustrated in Fig. 7, the internal resistance R_s of the C@$NiCo_2S_4$ and C@$NiCo_2S_4$–H nanorods was measured to be 0.66 and 0.72 Ω, respectively,

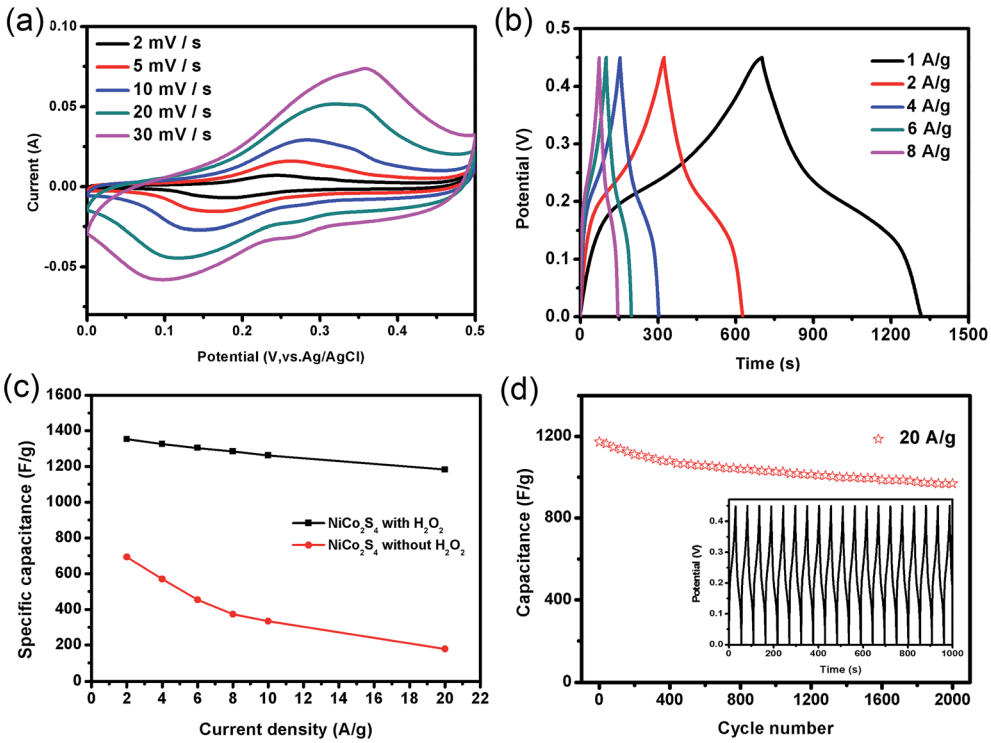

Fig. 6 Electrochemical performance of C@$NiCo_2S_4$–H nanorod. (a) *CV* curves at different scan rates. (b) Charge–discharge curves at different current densities. (c) Effects of current density on its specific capacitance. (d) Cycling performance of 2000 cycles at the current density of 20.0 A g^{-1}. The inset shows the last 20 cycles of charge–discharge curves.

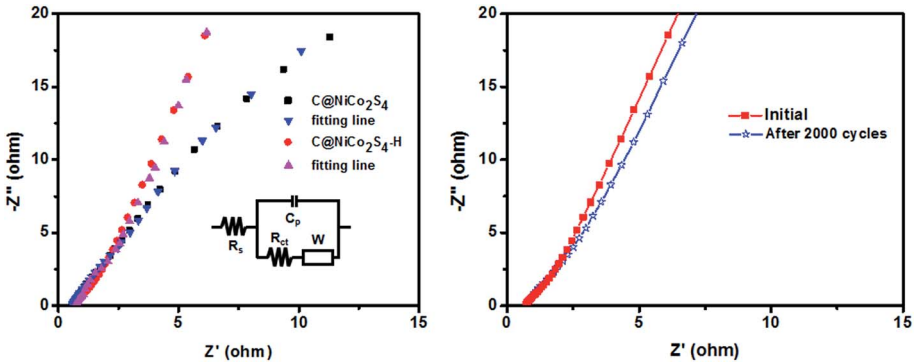

Fig. 7 (a) Nyquist plots of C@$NiCo_2S_4$ and C@$NiCo_2S_4$–H nanorod samples. (b) Nyquist plots of C@$NiCo_2S_4$–H nanorods before and after 2000 cycles.

whereas the charge transfer resistance R_{ct} was 5.02 and 3.49 Ω, respectively, demonstrating that C@$NiCo_2S_4$–H has lower resistance. In the low frequency range, the C@$NiCo_2S_4$–H nanorods present a more vertical line, indicating the better capacitive performance and the lower Warburg resistance (electrolyte diffusion impedance).[39] These results are in good agreement with the previously discussed *CV* and charge–discharge curves, which further reveals the better performance of the as-obtained C@$NiCo_2S_4$–H nanorods. Fig. 7b shows the Nyquist plots of C@$NiCo_2S_4$–H nanorods before and after 2000 cycles. As seen from the figure, the EIS characteristics were barely changed, confirming the excellent stability of the electrode during a fast reversible redox reaction.

Conclusion

In this study, a facile hydrothermal method for the fabrication of carbon@$NiCo_2S_4$ nanorods was proposed with Ni/C nanorods as the support. After in-depth study and data analysis, it was found that the specific surface area of the C@$NiCo_2S_4$ nanorod could be effectively engineered through the addition of H_2O_2 during the synthesis. As a supercapacitor electrode, the performance was greatly enhanced due to its modified structure and the synergistic effect of carbon nanorods and $NiCo_2S_4$. Moreover, 83% of its initial capacitance can be retained even after 2000 consecutive charge–discharge cycles carried out at 20 A g^{-1}. The advanced supercapacitor material developed in this study demonstrates promising application potential for the design of high-performance energy conversion and storage devices in the future, while casting new light on the development of trinary transition metal sulfides.

Acknowledgements

The project was supported by the 973 program (2014CB660808), the Key University Science Research Project of Jiangsu Province (15KJA430006), the Jiangsu Provincial Founds for Distinguished Young Scholars (BK20130046), the NNSF of China (21275076, 61328401), the Program for New Century Excellent Talents in University (NCET-13-0853), the Qing Lan Project, the Synergetic Innovation Center for Organic Electronics and Information Displays, and the Priority Academic Program Development of Jiangsu Higher Education Institutions (PAPD).

References

1 P. Simon and Y. Gogotsi, *Nature*, 2008, **7**, 845.
2 L. Bao, J. Zang and X. Li, *Nano Lett.*, 2011, **11**, 1215.
3 B. E. Conway, *J. Electrochem. Soc.*, 1991, **138**, 1539.
4 M. Winter and R. J. Brodd, *Chem. Rev.*, 2004, **104**, 4245.
5 L. L. Zhang and X. S. Zhao, *Chem. Soc. Rev.*, 2009, **38**, 2520.
6 Y. Chen, B. Qu, L. Hu, Z. Xu, Q. Li and T. Wang, *Nanoscale*, 2013, **5**, 9812.
7 N. Xiao, X. Dong, L. Song, D. Liu, Y. Tay, S. Wu, L.-J. Li, Y. Zhao, T. Yu, H. Zhang, W. Huang, H. H. Hng, P. M. Ajayan and Q. Yan, *ACS Nano*, 2011, **5**, 2749.
8 Y. Zhang, L. Li, H. Su, W. Huang and X. Dong, *J. Mater. Chem. A*, 2015, **3**, 43.
9 Z. Wu, Y. Zhu and X. Ji, *J. Mater. Chem. A*, 2014, **2**, 14759.
10 G. Zhang and X. W. Lou, *Adv. Mater.*, 2013, **25**, 976.
11 N. Padmanathan and S. Selladurai, *Ionics*, 2013, **20**, 479.
12 Y. Xu, X. Wang, C. An, Y. Wang, L. Jiao and H. Yuan, *J. Mater. Chem. A*, 2014, **2**, 16480.
13 S. Peng, L. Li, H. B. Wu, S. Madhavi and X. W. D. Lou, *Adv. Energy Mater.*, 2015, **5**, 1401172.
14 J. Haetge, I. Djerdj and T. Brezesinski, *Chem. Commun.*, 2012, **48**, 6726.
15 S. J. Peng, L. L. Li, C. C. Li, H. T. Tan, R. Cai, H. Yu, S. Mhaisalkar, M. Srinivasan, S. Ramakrishna and Q. Y. Yan, *Chem. Commun.*, 2013, **49**, 10178.
16 X. Wang, X. Han, M. Lim, N. Singh, C. L. Gan, M. Jan and P. S. Lee, *J. Phys. Chem. C*, 2012, **116**, 12448.
17 L. Chen, X. Zhang, H. Liang, M. Kong, Q. Guan, P. Chen, Z. Wu and S. Yu, *ACS Nano*, 2012, **6**, 7092.
18 B. B. Garcia, S. L. Candelaria and G. Cao, *J. Mater. Sci.*, 2012, **47**, 5996.
19 Z. Xing, Q. Chu, X. Ren, J. Tian, A. M. Asiri, K. A. Alamry, A. O. Al-Youbi and X. Sun, *Electrochem. Commun.*, 2013, **32**, 9.
20 J. Xiao, L. Wan, S. Yang, F. Xiao and S. Wang, *Nano Lett.*, 2014, **14**, 831.
21 L. Yu, B. Yang, Q. Liu, J. Liu, X. Wang, D. Song, J. Wang and X. Jing, *J. Electroanal. Chem.*, 2015, **739**, 156.

22 H.-Y. Wang, F.-X. Xiao, L. Yu, B. Liu and X. W. Lou, *Small*, 2014, **10**, 3181.
23 R. Zou, Z. Zhang, M. F. Yuen, J. Hu, C. S. Lee and W. Zhang, *Sci. Rep.*, 2015, **5**, 7862.
24 H. Wan, J. Jiang, J. Yu, K. Xu, L. Miao, L. Zhang, H. Chen and Y. Ruan, *CrystEngComm*, 2013, **15**, 7649.
25 C. Sun, M. Ma, J. Yang, Y. Zhang, P. Chen, W. Huang and X. Dong, *Sci. Rep.*, 2014, **4**, 7054.
26 X. Bo, L. Zhu, G. Wang and L. Guo, *J. Mater. Chem.*, 2012, **22**, 5758.
27 Y. Zhang, M. Ma, J. Yang, C. Sun, H. Su, W. Huang and X. Dong, *Nanoscale*, 2014, **6**, 9824.
28 C. Li, B. Zhan, C. Sun, M. Ma, X. Dong and W. Huang, *RSC Adv.*, 2014, **4**, 32047.
29 T. Wazawa, A. Matsuoka, G. Tajima, Y. Sugawara, K. Nakamura and K. Shikama, *Biophys. J.*, 1992, **63**, 544.
30 W. J. Dong, X. B. Wang, B. J. Li, L. N. Wang, B. Y. Chen, C. R. Li, X. A. Li, T. R. Zhang and Z. Shi, *Dalton Trans.*, 2011, **40**, 243.
31 L. Mei, T. Yang, C. Xu, M. Zhang, L. Chen, Q. Li and T. Wang, *Nano Energy*, 2014, **3**, 36.
32 Z. Tang, C.-h. Tang and H. Gong, *Adv. Funct. Mater.*, 2012, **22**, 1272.
33 X. Liu, Q. Long, C. Jiang, B. Zhan, C. Li, S. Liu, Q. Zhao, W. Huang and X. Dong, *Nanoscale*, 2013, **5**, 6525.
34 Y. Zhang, M. Ma, J. Yang, W. Huang and X. Dong, *RSC Adv.*, 2014, **4**, 8466.
35 J. Yang, M. Ma, C. Sun, Y. Zhang, W. Huang and X. Dong, *J. Mater. Chem. A*, 2015, **3**, 1258.
36 Y. Zhang, M. Ma, J. Yang, C. Sun, H. Su, W. Huang and X. Dong, *Nanoscale*, 2014, **6**, 9824.
37 H. C. Chen, J. J. Jiang, Y. D. Zhao, L. Zhang, D. Q. Guo and D. D. Xia, *J. Mater. Chem. A*, 2015, **3**, 428.
38 K.-P. Wang and H. Teng, *J. Electrochem. Soc.*, 2007, **154**, A993.
39 L. Wang, Z. H. Dong, Z. G. Wang, F. X. Zhang and J. Jin, *Adv. Funct. Mater.*, 2013, **23**, 275.